2

SPECTRA AND COSPECTRA OVER
FLAT UNIFORM TERRAIN

Turbulent flows like those in the atmospheric boundary layer can be thought of as a superposition of eddies—coherent patterns of velocity, vorticity, and pressure—spread over a wide range of sizes. These eddies interact continuously with the mean flow, from which they derive their energy, and also with each other. The large "energy-containing" eddies, which contain most of the kinetic energy and are responsible for most of the transport in the turbulence, arise through instabilities in the background flow. The random forcing that provokes these instabilities is provided by the existing turbulence. This is the process represented in the production terms of the turbulent kinetic energy equation (1.59) in Chapter 1.

The energy-containing eddies themselves are also subject to instabilities, which in their case are provoked by other eddies. This imposes upon them a finite lifetime before they too break up into yet smaller eddies. This process is repeated at all scales until the eddies become sufficiently small that viscosity can affect them directly and convert their kinetic energy to internal energy (heat). The action of viscosity is captured in the dissipation term of the turbulent kinetic energy equation.

The second-moment budget equations presented in Chapter 1, of which (1.59) is one example, describe the summed behavior of all the eddies in the turbulent flow. To understand the conversion of mean kinetic energy into turbulent kinetic energy in the large eddies, the handing down of this energy to eddies of smaller and smaller scale in an "eddy cascade" process, and its ultimate conversion to heat by viscosity, we must isolate the different scales of turbulent motion and separately observe their behavior. Taking Fourier spectra and cospectra of the turbulence offers a convenient way of doing this. The spectral representation associates with each scale of motion the amount of kinetic energy, variance, or eddy flux it contributes to the whole and provides a new and invaluable perspective on boundary layer structure.

The spectrum of boundary layer fluctuations covers a range of more than five decades: millimeters to kilometers in spatial scales and fractions of a second to

hours in temporal scales. The field experiments of the last two decades confirm that spectral representations in the wavenumber or frequency domain follow similarity laws much like the time-averaged statistics discussed in Chapter 1. When nondimensionalized with the appropriate scaling parameters (u_*, T_*, w_*, and θ_*), the spectral and cospectral forms reduce to a set of universal curves that are functions only of z/L in the surface layer and z/z_i in the convective mixed layer. The existence of such order in the spectral domain is indeed gratifying to the boundary layer meteorologist. On a practical level, it provides engineers and modelers with the equations they need for a range of applications, from design of structures to air pollution predictions. In the ABL, the experimenter can use that information to determine the frequency requirements for sensors operating at a given height or, conversely, to adjust the observing height to suit the response characteristics of available sensors.

    This chapter assumes familiarity with the general principles of the application of Fourier transforms to random processes. The essential formulas are presented in Appendix 2.1.

2.1   Spectral characteristics of boundary layer turbulence

The turbulent eddies we observe in the boundary layer are spatially extensive structures, and, ideally, their analysis requires information from many points in space. Such measurements are becoming increasingly available from aircraft and remote sensors, but the greater part of the data available to the micrometeorologist is still derived from point measurements in space as a function of time. To convert these temporal measurements into spatially distributed data, we commonly adopt Taylor's frozen turbulence hypothesis, which assumes that eddies change imperceptibly as they are convected by the mean wind $\overline{u}$ past an in situ sensor (Appendix 2.2). This assumption works best in the surface layer and worst in the high-intensity turbulence of a plant canopy or in the mixed layer. (In the recirculating flow behind a hill, it does not work at all.)

    With two sensors a distance r apart, we can form the two-point covariance tensor R_{ij} ($\mathbf{x,r}$) that provides the fundamental description of spatial structure in the turbulence

$$R_{ij}(\mathbf{x, r}) = \overline{u_i'(\mathbf{x})u_j'(\mathbf{x + r})}. \qquad (2.1)$$

    The Fourier transform of $R_{ij}(\mathbf{x,r})$ converts that covariance to a two-point spectrum tensor $E_{ij}(\mathbf{x},\kappa)$, where κ represents the wavenumber vector. $E_{ij}(\mathbf{x},\kappa)$ contains complete information on the distribution of turbulent variance and covariance over wavenumber space. Unfortunately, more information on the flow structure than we usually possess is required to form either $E_{ij}(\mathbf{x}, \kappa)$ or $R_{ij}(\mathbf{x, r})$ and we usually work with simpler and more attainable descriptions.
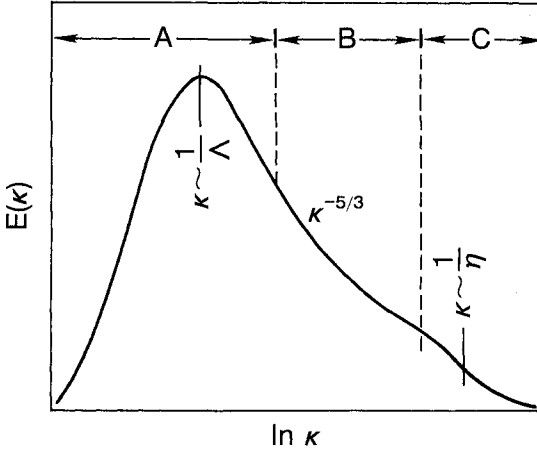
FIG. 2.1. Schematic of energy spectrum in the atmospheric boundary layer showing distinct regions of energy production (A) and dissipation (C) and the inertial subrange (B), where both energy production and dissipation are negligible. Λ is the integral scale of turbulence and η is the Kolmogorov microscale.

A particularly useful conceptual picture of the distribution of energy in wavenumber space, if we are dealing with turbulence that is homogeneous in all directions, is provided by the scalar energy spectrum $E(\kappa)$. $E(\kappa)$ represents the contribution to the total kinetic energy from Fourier modes with wavenumber magnitudes between κ and $\kappa + d\kappa$, where $\kappa = |\kappa|$. For a precise definition of $E(\kappa)$, see Lumley and Panofsky (1964). $E(\kappa)$ peaks in the energy-containing region, by definition, and drops to zero at both ends of the spectrum. In its schematic representation in Fig. (2.1) we identify the three major spectral regions, A, B, and C, relevant to boundary layer flow.

A The *energy-containing range*, which contains the bulk of the turbulent energy and where energy is produced by buoyancy and shear.

B The *inertial subrange*, where energy is neither produced nor dissipated but handed down to smaller and smaller scales.

C The *dissipation range*, where kinetic energy is converted to internal energy.

The energy-containing and dissipation ranges have their own characteristic length scales: In the former it is the Eulerian integral length scale Λ; in the latter, the so-called Kolmogorov microscale η. In Fig. 2.1 we show $E(\kappa)$ reaching its maximum at a wavenumber corresponding roughly to the Eulerian integral length scale[1]

---

[1] We cannot be more precise because $E(\kappa)$ is not easily measured in the atmosphere. Also, there is no simple relationship between $R_{ij}(\mathbf{x}, \mathbf{r})$ and $E(\kappa)$ except in fully isotropic turbulence (Batchelor, 1960), where the spectrum can be shown to peak at $\sqrt{\pi}/\Lambda$, close enough for our approximation of $1/\Lambda$.

$(\kappa \sim 1/\Lambda)$. With a single sensor and the use of Taylor's hypothesis, we are constrained to define that integral length scale in terms of its components Λ_u, Λ_v, and Λ_w, derived from the integral time scales $\mathcal{T}_u$, $\mathcal{T}_v$, and $\mathcal{T}_w$, available from our measurements of u, v, and w. These integral time scales actually represent the time scales over which the turbulence remains correlated (Fig. 2.2).

Taking Λ_u as an example we can write

$$\Lambda_u = \overline{u}\mathcal{T}_u = \overline{u}\int_0^\infty \rho_u(\xi) = \overline{u}\int_0^\infty \frac{\overline{u'(t)u'(t+\xi)}}{\sigma_u^2}\, d\xi, \tag{2.2}$$

where $\rho_u(\xi)$ is the autocorrelation function as defined above, ξ the time lag with respect to time t (Fig. 2.2), and $\overline{u}$ the mean wind velocity. If $\rho_u(\xi)$ is an exponential function, the integral time scale is the value of ξ at $\rho_u(\xi) = 1/e \simeq 0.37$ ($e \simeq 2.72$, the base for natural logarithms). For a discussion of autocorrelation functions and integral time scales, see Appendix 7.2 in Chapter 7.

In the dissipation range the scaling length η is given by

$$\eta = \left(\frac{\nu^3}{\epsilon}\right)^{1/4},$$

where ν is the kinematic viscosity of air and ϵ is the dissipation rate of turbulent kinetic energy. Whereas Λ_u varies typically from 10 to 500 m, η is of the order of 0.001 m.
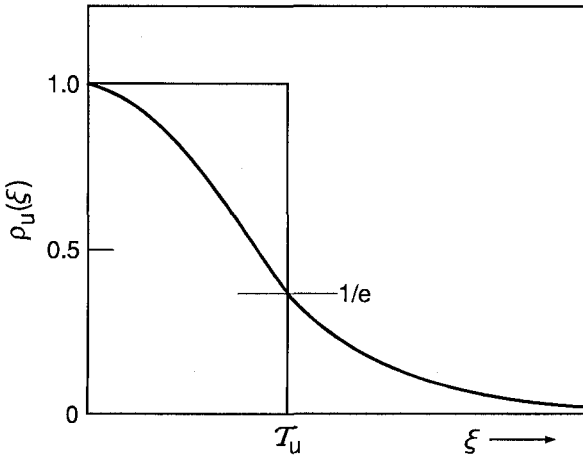

FIG. 2.2. Autocorrelation function and its relation to the integral time scale $\mathcal{T}_u$. The 1/e point on the curve is usually a good approximation of the integral time scale even when the correlation function is not strictly exponential. [The area under the rectangle should equal the area under $\rho_u(\xi)$.]

In the inertial subrange, energy is neither produced nor dissipated, and the transfer of energy from the energy-containing to the dissipation range is controlled entirely by ϵ, the rate at which energy is converted to heat in the dissipation range. Here, the form of the spectrum can be deduced from purely dimensional arguments (Kolmogorov, 1941).

Adopting Taylor's hypothesis implies a natural relationship between wavenumbers and frequencies. All our observations are henceforth defined in terms of the streamwise wavenumber κ_1 (subscript 1 for component in the streamwise direction), which corresponds to $2\pi/\lambda$, where λ is the wavelength approximated by $\overline{u}/f$, f being the cyclic frequency. The one-dimensional spectra $F_u(\kappa_1), F_v(\kappa_1)$, and $F_w(\kappa_1)$ of the three wind velocity components (available to us through spectrum analysis of measurements from fixed sensors) have forms somewhat different from $E(\kappa)$ but are predictable nevertheless in both the inertial subrange and the energy-containing region.

2.2   Inertial subrange

Kolmogorov, who first conceived the idea of an inertial subrange separating the energy-containing and dissipation ranges, argued from dimensional considerations that $E(\kappa)$ in this region should be proportional to $\epsilon^{2/3}\kappa^{-5/3}$ (Kolmogorov, 1941). Here the u spectrum, in its familiar one-dimensional form, becomes

$$F_u(\kappa_1) = \alpha_1 \epsilon^{2/3} \kappa_1^{-5/3}, \qquad (2.3)$$

where α_1 is the Kolmogorov constant with a value estimated between 0.5 and 0.6. This is the well-known $-5/3$ power law for the inertial subrange. Theoretical arguments suggest that turbulence is isotropic in this range. Isotropy implies that the velocity field is independent of rotation and reflection about the spatial axes. Even though isotropy does not apply to the energy-containing eddies, we can assume that the small-scale ($\lambda \ll \Lambda_u$) structure is effectively isotropic. This *local isotropy* is important for the derivation of small-scale turbulence statistics. (*Local* in this context refers to wavenumber space not physical space.) If local isotropy exists in the inertial subrange, we have the following relationship among the u, v, and w spectra:

$$F_v(\kappa_1) = F_w(\kappa_1) = (4/3)F_u(\kappa_1), \qquad (2.4)$$

which is illustrated in Fig. 2.3. In this log-log representation of the spectra, power laws appear as constant slopes and ratios as fixed separations. The spectra for v and w are placed higher than u in the inertial subrange, where they all fall off as $\kappa_1^{-5/3}$. Another consequence of local isotropy is the vanishing of all correlations between velocity components and between the velocity components and scalars;
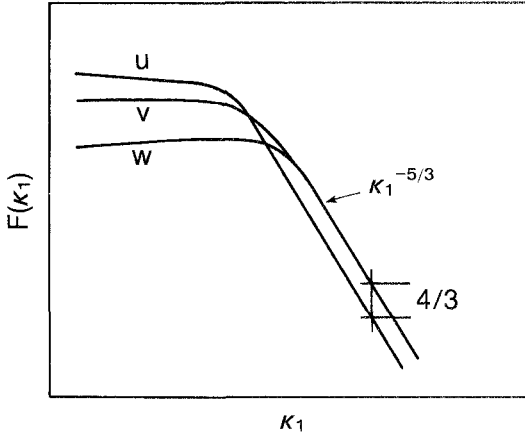
Fig.. 2.3. Idealized velocity spectra presented in log-log coordinates showing -5/3 slope in the inertial subrange and the 4/3 ratio between the transverse and streamwise velocity components.

this implies there can be no turbulent fluxes in the inertial subrange. The three conditions: $-5/3$ power law, $4/3$ ratio between transverse and longitudinal velocity components, and vanishing (or very low) cospectral levels are used as a test for the existence of an inertial subrange. [The ability to reach well into this region of the spectrum through the use of sonic anemometers (Chapter 6) to confirm these inertial subrange properties was critical to later development of universal forms for ABL spectra.] The $-5/3$ power law extends approximately to wavenumber $\kappa_1 = 0.1\eta^{-1}$ (Dubovikov and Tatarskii, 1987), above which it begins to fall off sharply with increasing κ_1.

Corrsin (1951) proposed an inertial subrange form for the temperature spectrum that appears to be valid for other scalars such as humidity:

$$F_\theta(\kappa_1) = \beta_1 \epsilon^{-1/3} N_\theta \kappa_1^{-5/3}, \tag{2.5}$$

where N_θ is the dissipation rate for half the temperature variance and β_1 is a universal constant with a value about 0.8 (Kaimal et al., 1972). [Note that at high wavenumbers approaching the dissipation range, the temperature spectrum exhibits a "bump" due to straining effects on the temperature eddies (Hill, 1978) not observed in the velocity spectra.]

2.3   Energy-containing range

The spectral forms in the energy-containing range tend to be different for each variable, since the integral scales they respond to are different. Yet they all seem

to behave in a consistent manner when plotted in dimensionless similarity coordinates.

Implicit in the development of spectral forms in this range is the assumption that a spectral gap exists, separating boundary layer turbulence from external fluctuations. Fortunately for the meteorologist, a spectral gap of sorts can often be found in the CBL at a frequency f between 0.001 and 0.0001 Hz, between the convection-driven boundary layer scales and the synoptic scales (Van der Hoven, 1957). This end of the spectrum, however, is susceptible to contamination from long-term trends present in the data. These may be caused by gravity waves, diurnal variation, synoptically induced changes, or simply drift in the sensor. In the absence of such trends in the record, $F(\kappa_1)$ is seen to level off to a constant value as $\kappa_1 \to 0$, a consequence of the one-dimensional representation of the three-dimensional turbulence spectrum (see Appendix 2.3). Identifying energy peaks in this type of spectral plot is difficult. For a more realistic representation of peaks and valleys in the distribution of turbulent energy, meteorologists use the wavenumber-weighted form $\kappa_1 F(\kappa_1)$ of the spectrum. In Fig. 2.4 we see $\kappa_1 F(\kappa_1)$ for the u component peaking at $\kappa_1 \approx 1/\Lambda_u$ while falling off as κ_1^{+1} on the low side and $\kappa_1^{-2/3}$ on the high side.

The low-frequency spectrum can usually be approximated by one of two analytic forms:

$$\frac{\kappa_1 F_\alpha(\kappa_1)}{\sigma_\alpha^2} = \frac{A(\kappa_1/\kappa_{1m})}{1 + B(\kappa_1/\kappa_{1m})^{5/3}} \tag{2.6}$$
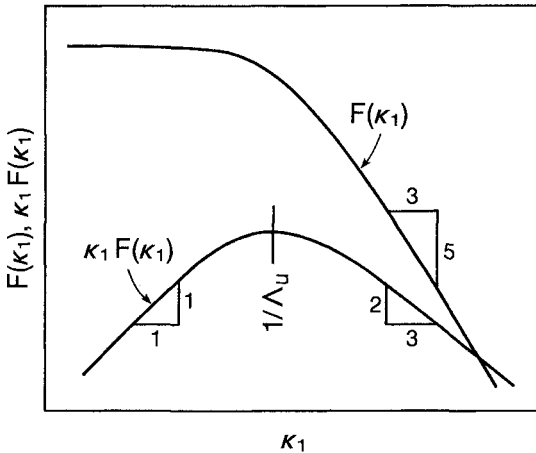

FIG. 2.4. Log-log representations of the frequency-weighted and unweighted power spectral densities. We show both plots in the same graph even though the two spectra have different dimensions (variance and variance/unit frequency interval) to compare their behavior as a function of κ_1.

or

$$\frac{\kappa_1 F_\alpha(\kappa_1)}{\sigma_\alpha^2} = \frac{C(\kappa_1/\kappa_{1m})}{[1 + D(\kappa_1/\kappa_{1m})]^{5/3}} \tag{2.7}$$

where $\alpha = u, v, w,$ or θ; $A, B, C,$ and D are adjustable constants, and the subscript m denotes κ_1 at the spectral peak. Equation (2.6) fits unstable w spectra and all the stable spectra. Equation (2.7) fits the unstable $u, v,$ and θ spectra slightly better than (2.6).

This wavenumber-weighted spectrum is also referred to as a logarithmic spectrum since it represents the variance per unit logarithmic wavenumber interval. Its units are those of variance (e.g., $m^2\ s^{-2}$) instead of variance per wavenumber interval $\Delta\kappa_1$ (as in the unweighted spectrum). Yet, when plotted on a log-log scale, power relationships appear as straight lines as with the unweighted spectrum, a distinct advantage when dealing with atmospheric spectra. The log-log plot is, however, not area-preserving since

$$\sigma_\alpha^2 = \int_0^\infty F_\alpha(\kappa_1)\, d\kappa_1 = \int_0^\infty \kappa_1 F_\alpha(\kappa_1)\, d(\ln \kappa_1).$$

For an equal area spectrum, $\kappa_1 F_\alpha(\kappa_1)$ should be plotted on a linear scale and κ_1 on a log scale, but power laws will not be straight lines on that plot.

2.4   Conversion from wavenumber to frequency scales

Although spectral theories are formulated in wavenumber space, most measurements are performed in frequency space. To convert spatial scales to frequency scales we invoke Taylor's hypothesis, $\kappa_1 = 2\pi f/\overline{u}$, where f is the cyclic frequency as defined earlier.

Taking the u spectrum as an example, we have

$$\int_0^\infty F_u(\kappa_1)\, d\kappa_1 = \sigma_u^2 = \int_0^\infty S_u(f)\, df. \tag{2.8}$$

We use a different symbol to represent the frequency spectrum. If $\kappa_1 = 2\pi f/\overline{u}$, we have

$$\frac{2\pi}{\overline{u}} F_u\left(\frac{2\pi f}{\overline{u}}\right) = S_u(f), \tag{2.9}$$

or

$$\kappa_1 F_u(\kappa_1) = f S_u(f). \tag{2.10}$$

It can be shown that the relationship in (2.10) holds for any form of f, including the nondimensional frequency $n(= fz/\overline{u})$, used in surface layer work. Thus, $\kappa_1 F_u(\kappa_1)$, $fS_u(f)$, and $nS_u(n)$ all represent the same numerical value, allowing us considerable freedom in choosing frequency scales for the abscissa. For example, $fS(f)$ can be plotted as a function of κ_1, f, or n, without any conversion of units.

2.5   Surface layer spectra

Following conventions established for M-O scaling, we use u_* and T_* for nondimensionalizing velocity and temperature spectra in the surface layer. The appropriate dimensionless frequency scale for representing spectra would be $n = fz/\overline{u}$, which is the ratio of height z to wavelength λ. We also recall the dimensionless form for ϵ introduced in Chapter 1:

$$\phi_\epsilon = \frac{kz\epsilon}{u_*^3}, \tag{2.11}$$

which, according to similarity theory, should be a function only of z/L.

We start with the inertial subrange u spectrum expressed in the framework of surface layer similarity,

$$\begin{aligned}
\frac{fS_u(f)}{u_*^2} &= \frac{\alpha_1}{(2\pi)^{2/3}} \left(\frac{\epsilon^{2/3} z^{2/3}}{u_*^2} \right) \left(\frac{fz}{\overline{u}} \right)^{-2/3} \\
&= \frac{\alpha_1}{(2\pi k)^{2/3}} \phi_\epsilon^{2/3} \left(\frac{fz}{\overline{u}} \right)^{-2/3}
\end{aligned} \tag{2.12}$$

Denoting the dimensionless frequency $fz/\overline{u}$ by n and using values $\alpha_1 = 0.55$ and $k = 0.4$ (see Appendix 2.4), we have (Kaimal et al., 1972)

$$\frac{fS_u(f)}{u_*^2 \phi_\epsilon^{2/3}} = 0.3\, n^{-2/3} \tag{2.13}$$

When plotted on a log-log scale, the inertial subrange spectra collapse to a single straight line with a $-2/3$ slope. All the variability in the ordinate is absorbed in $\phi_\epsilon^{2/3}$. We have from Chapter 1 the functional form for $\phi_\epsilon^{2/3}$:

$$\phi_\epsilon^{2/3} = \begin{cases} 1 + 0.5|z/L|^{2/3}, & z/L \leq 0 \\ (1 + 5z/L)^{2/3}, & z/L \geq 0 \end{cases} \tag{2.14}$$

The dimensionless spectra for the remaining velocity components and temperature can similarly be expressed as

$$\frac{fS_v(f)}{u_*^2 \phi_\epsilon^{2/3}} = 0.4\, n^{-2/3}, \tag{2.15}$$

$$\frac{fS_w(f)}{u_*^2 \phi_\epsilon^{2/3}} = 0.4\,n^{-2/3}, \tag{2.16}$$

$$\frac{fS_\theta(f)}{T_*^2 \phi_N \phi_\epsilon^{-1/3}} = 0.43\,n^{-2/3}. \tag{2.17}$$

For the temperature spectrum in (2.17) we assumed $\beta_1 = 0.8$. In Chapter 1 we defined the similarity function for N_θ as

$$\phi_N = \frac{kzN_\theta}{u_* T_*^2}. \tag{2.18}$$

Also, in the temperature variance budget, we found a local balance between the production and destruction of temperature variance ($N_\theta \simeq -\overline{w'\theta'}\partial\overline{\theta}/\partial z$), which suggests that $\phi_N \simeq \phi_h$. Hence (2.17) can be expressed in terms of ϕ_h as

$$\frac{fS_\theta(f)}{T_*^2 \phi_h \phi_\epsilon^{-1/3}} \simeq 0.43n^{-2/3}. \tag{2.19}$$

With the velocity and temperature spectra anchored to the inertial subrange formulations of (2.13), (2.15), (2.16), and (2.17), we can now examine the rest of the spectrum to see if it will collapse into a narrow band (as in the inertial subrange) or progress in some orderly fashion as a function of z/L. The plots for the four variables from the Kansas experiment (Kaimal et al., 1972) are given in Figs. 2.5–2.8. Of the four, the w spectrum exhibits the most systematic variation with z/L;
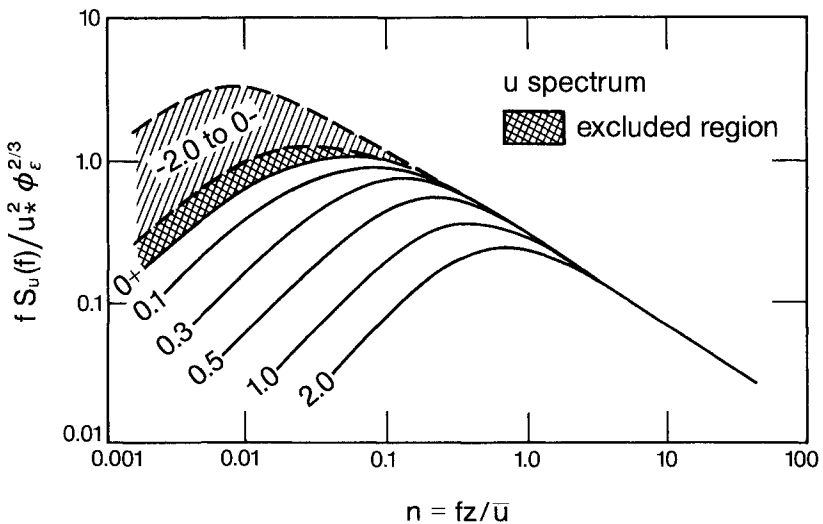

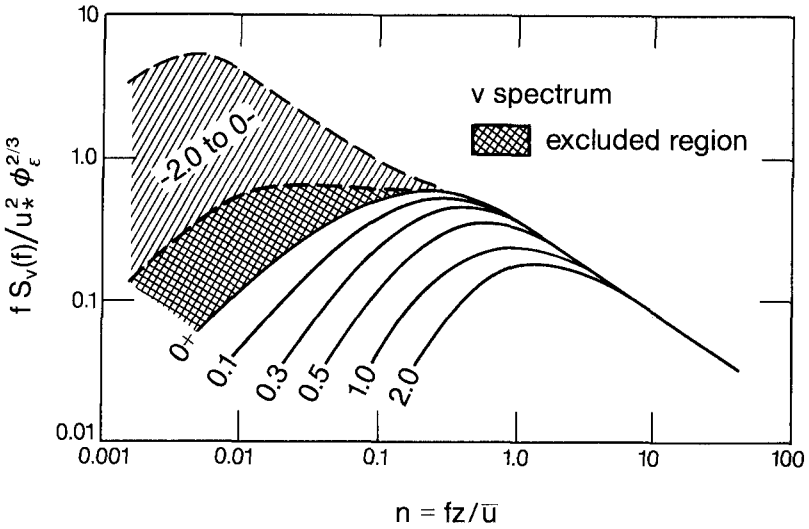FIG. 2.5. Normalized surface layer u spectrum shown varying with z/L.

FIG. 2.6. Normalized surface layer v spectrum shown varying with z/L.

only in the range $-0.3 > z/L > -2$ (shown as a hatched area in Fig. 2.7) does the spectrum exhibit an insensitivity to z/L. This happens because the normalized spectral peak n_m stops shifting to lower frequencies with increasing z/L (see Fig. 2.9), an indication that the peak wavelength λ_m scales only with z. The u, v, and θ stable spectra also progress systematically, but their unstable spectra spread over a
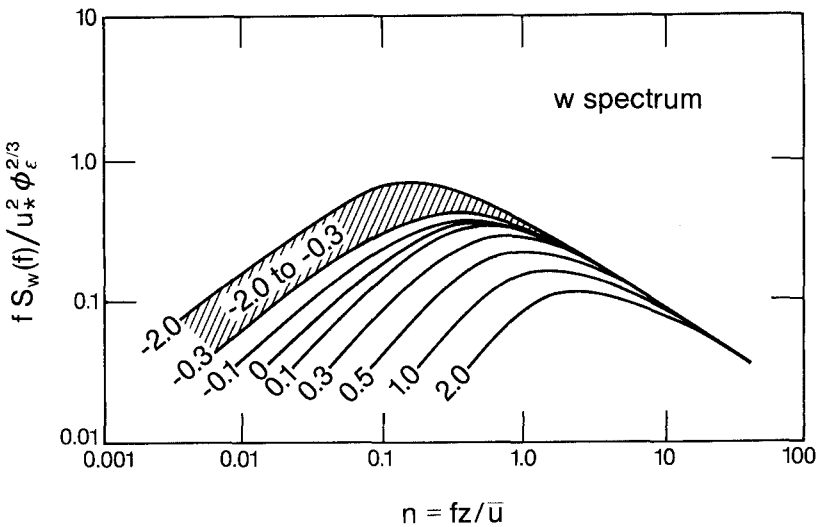

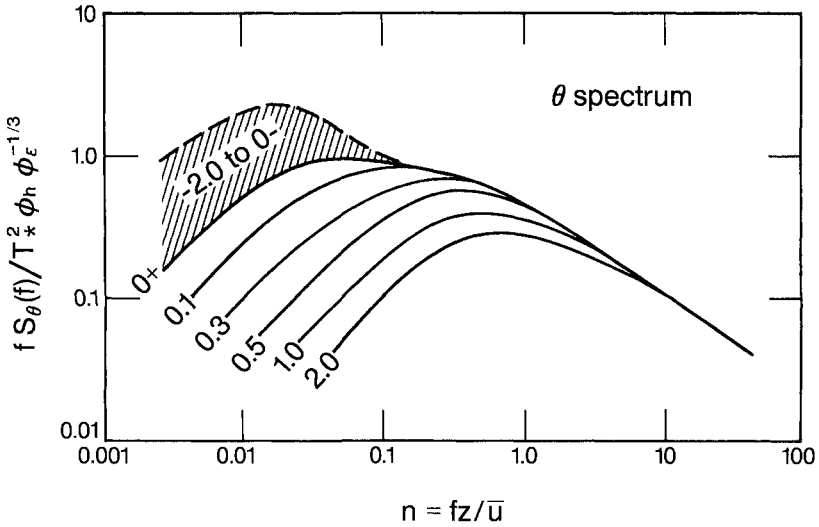FIG. 2.7. Normalized surface layer w spectrum shown varying with z/L.

FIG. 2.8. Normalized surface layer θ spectrum shown varying with z/L.

larger area (hatched); in u and v, an "excluded" region (crosshatched) can be seen separating the stable and unstable spectra. The limiting curves for stability regimes approaching neutral from both sides are indicated by notations $z/L = 0+$ and $0-$ in the figures. Clearly, the unstable u and v spectra do not follow M-O similarity, and since no measurements of the boundary layer depth z_i were made in Kansas, it was not known at the time that their λ_m's scaled with z_i. Later, the Minnesota
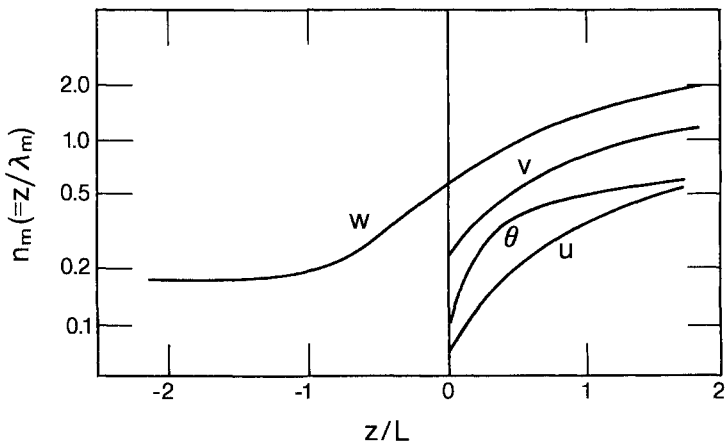

FIG. 2.9. Nondimensionalized frequency at spectral maxima shown as functions of z/L. For u, v, and θ, the curves are discontinuous at $z/L = 0$ and therefore valid only to $z/L = 0+$, the neutral limit on the stable side.

experiment (Kaimal et al., 1976) and the laboratory work of Willis and Deardorff (1974) revealed λ_m to be approximately $1.5z_i$. The wavelength at the spectral peak λ_m is a length scale of greater importance to boundary layer meteorologists than the integral length scale Λ since it is representative of the size of the eddies with the most energy. In Fig. 2.9, λ_m is presented in its dimensionless form z/λ_m, or n_m. On the stable side, we find n_m for all variables increasing rapidly with z/L. On the unstable side, only n_m for w decreases systematically with $-z/L$, approaching its free-convection limit of $n_m = 0.17$ at $z > -L$. (The unstable θ spectral peaks tend to be less predictable than the w peaks.)

The behavior of $(\lambda_m)_w$ in the surface layer and in the layer immediately above may be expressed as follows:

$$(\lambda_m)_w = \begin{cases} z(0.55 - 0.38|z/L|)^{-1}, & 0 \leq z \leq -L \\ 5.9z, & -L \leq z \leq 0.1z_i \end{cases} \tag{2.20}$$

$$(\lambda_m)_w = \begin{cases} z(0.55 + z/L)^{-1}, & 0 \leq z \leq L \\ zL(0.45z + 1.1L)^{-1}, & L \leq z \leq 2L \\ L, & z \geq 2L. \end{cases} \tag{2.21}$$

The free-convection form for $(\lambda_m)_w$ leads to the familiar approximation $\Lambda_w \sim z$ used in the lower boundary layer, where $(\lambda_m)_w$ is typically six to seven times larger than Λ_w. The tendency for $(\lambda_m)_w$ to become independent of z as z exceeds $2L$ on the stable side is consistent with Wyngaard and Coté's (1972) "z-less stratification" concept mentioned in Chapter 1.

The stable spectra exhibit a common form when normalized by their variances and plotted against the dimensionless frequency f/f_0; f_0 is the value of f where the extrapolated inertial subrange meets the $fS_\alpha(f)/\sigma_\alpha^2 = 1$ line (see Fig. 2.10). The spectra for u, v, w, and θ conform to the shape (Kaimal, 1973)

$$\frac{fS_\alpha(f)}{\sigma_\alpha^2} = \frac{0.164f/f_0}{1 + 0.164(f/f_0)^{5/3}}, \tag{2.22}$$

where $\alpha = u, v, w$, or θ.

By substituting for $fS_\alpha(f)$ from (2.13), (2.15), and (2.16) and assuming $\sigma_u/u_* = 2.17$, $\sigma_v/u_* = 1.78$, and $\sigma_w/u_* = 1.36$ from the Kansas stable data, Moraes (1988) showed

$$(f_0)_u = 0.012\phi_\epsilon, \tag{2.23}$$

$$(f_0)_v = 0.045\phi_\epsilon, \tag{2.24}$$
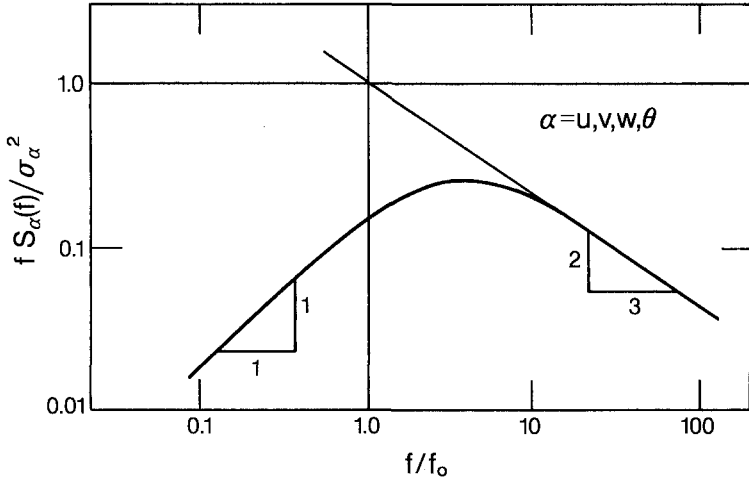
$$(f_0)_w = 0.094\phi_\epsilon. \tag{2.25}$$

FIG. 2.10. Normalized stable surface layer spectrum representing u, v, w, and θ. The abscissa is normalized by the frequency where the inertial subrange slope intercepts the $fS(f) = 1$ line, as shown in the figure.

The frequency f_0 is also related to the integral time scale T_α of the variable α since the low-frequency behavior of (2.22) is controlled by T_α (see Appendix 2.3).

The forms for u, v, and w most commonly used in engineering applications are the neutral Kansas spectra (Kaimal et al., 1972) shown in Fig. 2.11 with minor adjustments to provide the expected 4/3 ratio in the inertial subrange. They can be represented by

$$\frac{fS_u(f)}{u_*^2} = \frac{102n}{(1 + 33n)^{5/3}}, \tag{2.26}$$

$$\frac{fS_v(f)}{u_*^2} = \frac{17n}{(1 + 9.5n)^{5/3}}, \tag{2.27}$$

$$\frac{fS_w(f)}{u_*^2} = \frac{2.1n}{(1 + 5.3n^{5/3})}. \tag{2.28}$$

2.6 Mixed layer spectra

In the mixed layer, which comprises the upper 9/10 of the CBL, we find M-O similarity being replaced by a different scaling law: with z_i replacing $-L$, w_* replacing u_*, and θ_* replacing T_*, as we saw in Chapter 1. Since none of the new scaling parameters varies with height, we expect the spectra also to be invariant with height. In this new framework, λ_m, ϵ, and the magnitude of the $fS(f)$ peak will remain constant with height changing only from run to run in response to changes in $\overline{(w'\theta')}_0$ and z_i. This is indeed the case for u, v, and w spectra, as seen

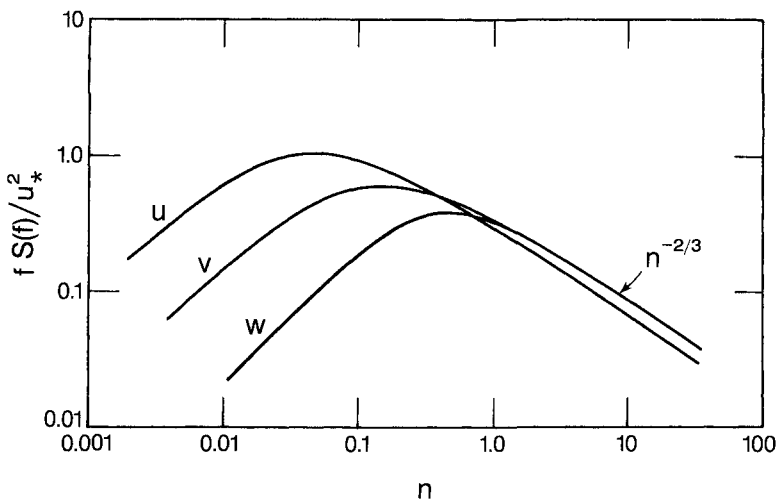**Fig. 2.11.** Normalized neutral ($z/L = 0+$) spectra for u, v, and w in the surface layer.
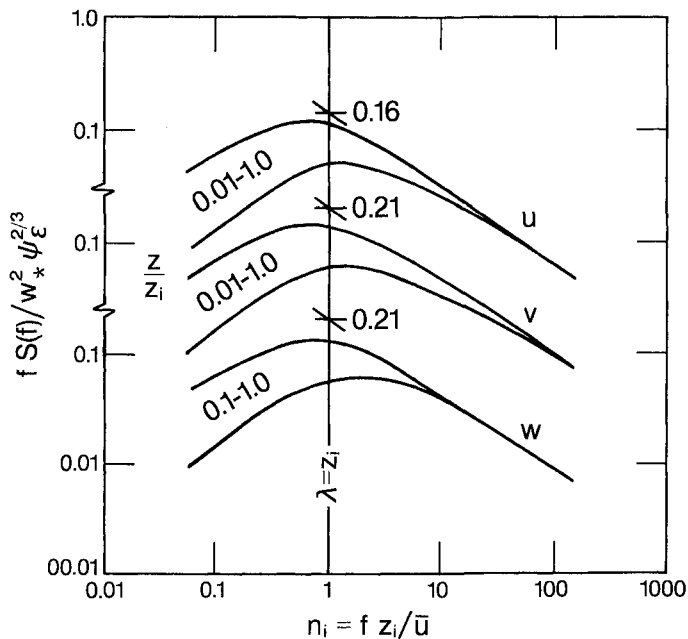

Fig. 2.12. Normalized mixed layer u, v, and w spectra. The two curves define the envelopes of spectra that fall within the z/z_i range indicated.

in their idealized representations in Fig. 2.12. Note that in the energy-containing range, w follows mixed layer similarity only down to $0.1z_i$, whereas u and v follow it almost all the way down.

The inertial subrange spectral form for u reduces to

$$\frac{fS_u(f)}{w_*^2} = \left[\frac{\alpha_1}{(2\pi)^{2/3}}\right] \psi_\epsilon^{2/3} \left(\frac{fz_i}{\overline{u}}\right)^{-2/3},$$

where $w_* = [(g/T)(\overline{w'\theta'})_0 z_i]^{1/3}$ and $\psi_\epsilon = \epsilon/(g/\overline{\theta})(\overline{w'\theta'})_0$, the ratio of dissipation rate to buoyant production rate near the surface. Representing $fz_i/\overline{u}$ by a new dimensionless frequency n_i and assuming $\alpha_1 = 0.55$, we can write (Kaimal et al., 1976)

$$\frac{fS_u(f)}{w_*^2\psi_\epsilon^{2/3}} = 0.16\,n_i^{-5/3}, \tag{2.29}$$

$$\frac{fS_v(f)}{w_*^2\psi_\epsilon^{2/3}} = 0.21\,n_i^{-5/3}, \tag{2.30}$$

$$\frac{fS_w(f)}{w_*^2\psi_\epsilon^{2/3}} = 0.21\,n_i^{-5/3}. \tag{2.31}$$

ψ_ϵ should have a value between 0.4 and 0.5 in the mixed layer if we assume negligible wind shear and a linear heat flux profile in the layer. The Minnesota data show ψ_ϵ ranging from 0.5 to 0.7, perhaps because of larger than expected shear production rates in some runs (Kaimal et al., 1976). Note that ψ_ϵ is identically the dimensionless dissipation rate $\epsilon z_i/w_*^3$ shown in Fig. 1.10.

The spectral peaks for u, v, and w are approximated as follows:

$$(\lambda_m)_u = (\lambda_m)_v = 1.5z_i, \qquad 0.01z_i \le z \le z_i \tag{2.32}$$

$$(\lambda_m)_w = \begin{cases} 5.9z, & -L \le z \le 0.1z_i \\ 1.8z_i(1 - e^{-4z/z_i} - 0.0003e^{8z/z_i}), & 0.1z_i \le z \le z_i. \end{cases} \tag{2.33}$$

The mixed layer form for $(\lambda_m)_w$, shown in Fig. 2.13, was derived by Caughey and Palmer (1979) from a combined plot of data from the Minnesota and Ashchurch experiments. The mixed layer $(\lambda_m)_\theta$ does not show a consistent pattern because the temperature fluctuations are generally small above the surface layer and easily overwhelmed by the effects of entrainment and the diurnal trend in the temperature. The profile of σ_θ^2 presented in Chapter 1 shows the variance decreasing to a minimum at about $0.6z_i$ and rising to its near-surface value at z_i, a clear demonstration of the influence of entrainment in the temperature statistics.
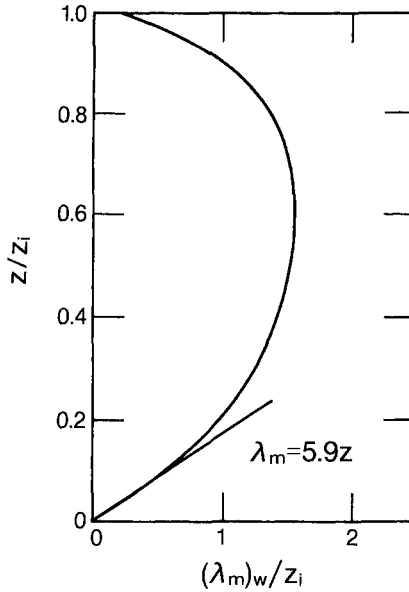
FIG. 2.13. Variation of the vertical velocity peak wavelength with height.

The evolution of u, v, w, and θ spectra with height in the ABL is shown schematically in Fig. 2.14. The u and v spectra appear flattened and stretched out in the surface layer as they adjust to conform to the mixed layer spectral forms of Fig. 2.12 in the energy-containing range and to the constraints of (2.13) and (2.15) in the inertial subrange. These spectra do not show much variation with height, except in the inertial subrange where the energy drops sharply with height in conformance with (2.14). The w spectrum, on the other hand, gains steadily in intensity as its peak moves down the frequency scale, consistent with the formulation in (2.20), and approaches the mixed layer form of Fig. 2.12 at $z = 0.2z_i$.

Two different approaches have been proposed to model this behavior of the u and v spectra. Kaimal (1978) used a simple interpolation formula linking the analytic form for the mixed layer spectrum

$$\frac{fS_u(f)}{\sigma_u^2} = n_i(1 + 3.1n_i^{5/3}) \qquad (2.34)$$

to the inertial subrange forms of (2.29), (2.30), and (2.31). Højstrup (1982) treated the u and v spectra as the sum of two spectra—a low-frequency spectrum scaling with z_i and a high-frequency spectrum scaling with z:
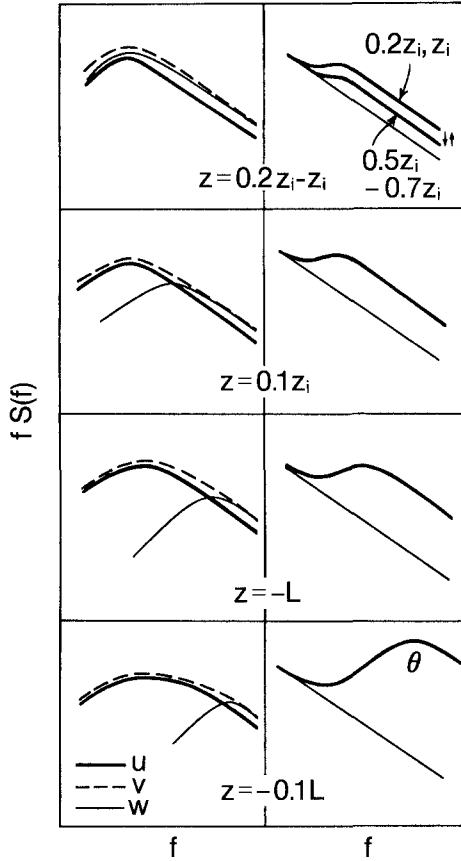
FIG. 2.14. Schematic representation of the evolution of spectra for velocity (left frames) and temperature (right frames) with height in the convective boundary layer. The thin reference line in the temperature plots is the spectrum of the diurnal trend.

$$\frac{fS_u(f)}{u_*^2} = \left[\frac{0.5n_i}{(1 + 2.2n_i^{5/3})}\right] \left(\frac{z_i}{|L|}\right)^{2/3} + \frac{102n}{(1 + 33n)^{5/3}}, \qquad (2.35)$$

$$\frac{fS_v(f)}{u_*^2} = \left[\frac{0.95n_i}{(1 + 2n_i^{5/3})}\right] \left(\frac{z_i}{|L|}\right)^{2/3} + \frac{17n}{(1 + 9.5n)^{5/3}}. \qquad (2.36)$$

The high-frequency contributions in (2.35) and (2.36) are identical to the Kansas forms in (2.26) and (2.27).

The modification of the θ spectrum with height is represented schematically in Fig. 2.14. The spectrum drops to its lowest point between $0.5z_i$ and $0.7z_i$, approaching spectral levels attributable to just the diurnal trend (used as reference in all the frames in Fig. 2.14); it rises again to its $z \approx 0.2z_i$ level at $z = z_i$. We can

express these shifts in terms of the inertial subrange behavior of the θ spectrum which, in the mixed layer framework, becomes

$$\frac{f S_\theta(f)}{\gamma \theta_*^2} = \frac{\beta_1}{(2\pi)^{2/3}} n_i^{-2/3} = 0.24 n_i^{-2/3}. \qquad (2.37)$$

$\theta_* = (\overline{w'\theta'})_0/w_*$, and γ is the nondimensional equivalent of $\psi_\epsilon^{2/3}$ in (2.29)–(2.31) given by

$$\gamma = \frac{N_\theta \epsilon^{-1/3}}{\theta_*^2 z_i^{-2/3}}. \qquad (2.38)$$

In the CBL, γ exhibits a profile with a predictable minimum at about $0.5z_i$. The Minnesota results (Kaimal et al., 1976) have been approximated by

$$\gamma = \begin{cases} 0.83(z/z_i)^{-4/3}, & z \le 0.5z_i \\ 2.1, & 0.5z_i \le z \le 0.7z_i \\ 6.1(z/z_i)^3, & 0.7z_i \le z \le z_i. \end{cases} \qquad (2.39)$$

We attribute the rise in the spectral energy above $0.7z_i$ to entrainment of warmer air from above the capping inversion into the mixed layer.

2.7   Stable outer layer spectra

In the stable outer layer (i.e., $h > z > L$, where L often ranges from 1/10 to 1/3 of the inversion depth h), the energy due to turbulence in the spectrum decreases rapidly with height, whereas that of the wave components present does not. At $z = h$, only the wave energy remains unless nonlinear processes induce wave breaking, thereby producing turbulent kinetic energy; at frequencies where turbulent energy shows a peak at the lower heights, the spectrum is flat and significantly depressed. (Note that Taylor's hypothesis does not apply to gravity waves as they are not transported by the mean wind.) A flat $fS(f)$ spectrum appears to be characteristic of stable atmospheric flows at $Ri \approx 0.2$ (Kaimal and Izumi, 1965; Okamoto and Webb, 1970); it represents a background noise containing equal energy per octave, analogous to the "pink noise" used in audio testing.

The evolution of u, v, w, and θ spectra with height in a hypothetical stable layer is shown schematically in Fig. 2.15. It is apparent that the vertical variations of λ_m cannot be generalized in any way because the stable outer layer is continually evolving (Caughey et al., 1979) and never reaching equilibrium. The positions and relative magnitudes of the turbulent peaks and the wave peaks can be expected to change with time in this layer. Examples of combined wave and turbulence spectra can be found in Finnigan et al. (1984).
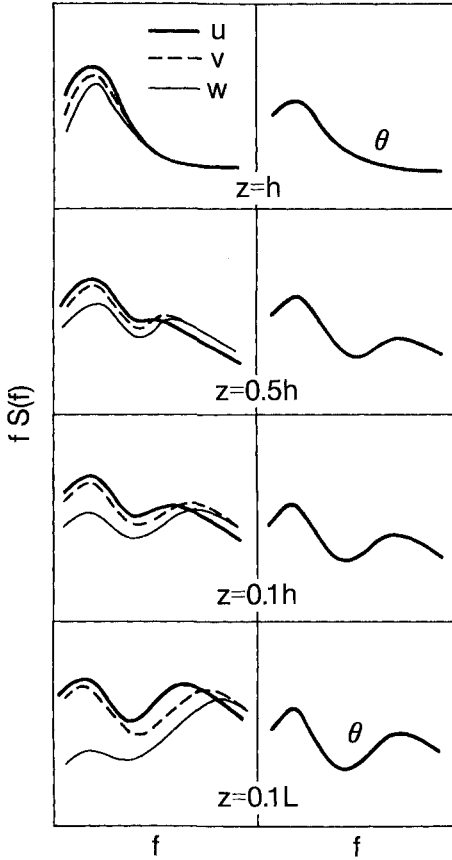
Fɪɢ. 2.15. Schematic representation of the evolution of spectra for velocity (left frames) and temperature (right frames) with height in the stable boundary layer.

2.8   Structure parameters and spectra

The structure parameter, a widely used indicator of the small-scale structure of turbulence in wave propagation studies, was originally defined in terms of the structure function $D(r)$ (Tatarski, 1961), where

$$D_\alpha(r) = \overline{[\alpha(x) - \alpha(x + r)]^2} = C_\alpha^2 r^{2/3}. \tag{2.40}$$

Here, C_α^2 is the structure parameter, α any variable (usually u, θ, or q), and r the distance separating two measurements of α along the x axis. It can be shown that C_α^2 is related to the one-dimensional spectrum of α through the relationship

$$F_\alpha(\kappa_1) = \frac{2C_\alpha^2}{3\Gamma(-1/3)} \kappa_1^{-5/3} \simeq 0.25 C_\alpha^2 \kappa_1^{-5/3}, \tag{2.41}$$

where Γ is the gamma function, provided the distance r is small enough to be within the range of length scales in the inertial subrange. The parameters, C_V^2, C_T^2, and C_Q^2 for u, θ, and q, respectively, are closely identified with C_n^2, the structure parameter of the refractive index for acoustic and electromagnetic waves propagating through the atmosphere. C_V^2 and C_T^2 are related to terms in the one-dimensional spectral forms for velocity and temperature as follows:

$$C_V^2 = 4\alpha_1 \epsilon^{2/3} \simeq 2.2\epsilon^{2/3}, \tag{2.42}$$

$$C_T^2 = 4\beta_1 N_\theta \epsilon^{-1/3} \simeq 3.2 N_\theta \epsilon^{-1/3}. \tag{2.43}$$

(The form for C_Q^2 is the same as for C_T^2, with the same numerical coefficient and the appropriate dissipation rate for humidity.) In the surface layer, the dimensionless forms for C_V^2 and C_T^2 may also be expressed in terms of ϕ functions defined earlier.

$$\frac{C_V^2 z^{2/3}}{u_*^2} = 2.2k^{-2/3}\phi_\epsilon^{2/3} = 4\phi_\epsilon^{2/3}, \tag{2.44}$$

$$\frac{C_T^2 z^{2/3}}{T_*^2} = 3.2k^{-2/3}\phi_N\phi_\epsilon^{-1/3} = 5.9\phi_N\phi_\epsilon^{-1/3}, \tag{2.45}$$

where $\phi_N = kzN_\theta/u_*T_*^2$ as in Chapter 1. For normalizing our temperature spectra we earlier assumed $\phi_N \simeq \phi_h$, but such a substitution in (2.45) would produce a form asymptotically incompatible with the $-4/3$ power law observed for γ at $z < 0.5z_i$. Instead we adopt the empirical form for C_T^2 derived directly from data (Wyngaard et al., 1971), adjusted to provide a good match with γ for $k = 0.4$. The form for $\phi_\epsilon^{2/3}$ in (2.14), in fact, evolves asymptotically to a constant in the lower mixed layer. Our formulations for the surface layer are

$$\frac{C_V^2 z^{2/3}}{u_*^2} = \begin{cases} 4(1 + 0.5|z/L|)^{2/3}, & z/L \leq 0 \\ 4(1 + 5z/L)^{2/3}, & z/L \geq 0 \end{cases} \tag{2.46}$$

$$\frac{C_T^2 z^{2/3}}{T_*^2} = \begin{cases} 5(1 + 6.4|z/L|)^{-2/3}, & z/L \leq 0 \\ 5(1 + 3z/L), & z/L \geq 0, \end{cases} \tag{2.47}$$

shown as functions of z/L in Fig. 2.16. Their mixed layer asymptotic forms are now

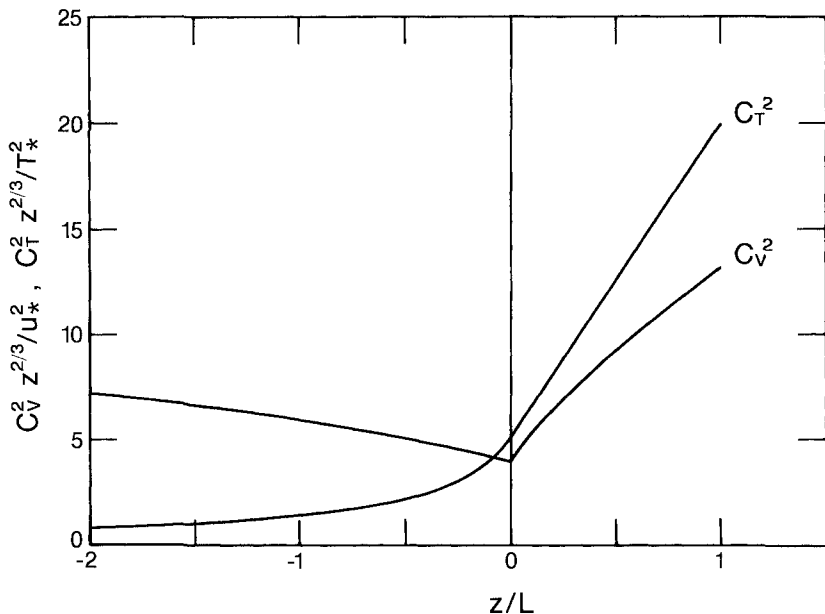$$\frac{C_V^2 z_i^{2/3}}{w_*^2} = 2.52k^{2/3} \simeq 1.4, \tag{2.48}$$

FIG. 2.16. Normalized structure parameters for velocity and temperature shown as functions of z/L.

$$\frac{C_T^2 z_i^{2/3}}{\theta_*^2} = 1.45 k^{-2/3} (z/z_i)^{-4/3} \simeq 2.7 \, (z/z_i)^{-4/3}. \tag{2.49}$$

The mixed layer profiles for C_V^2 and C_T^2 are presented in Fig. 2.17. Their evolution with height follows observations reported by Caughey and Palmer (1979). Of all the asymptotic power laws discussed so far, the form in (2.49) for C_T^2 shows the best fit with observations (Kaimal et al., 1976) over a very deep layer of the convective boundary layer. We do not have comparable asymptotic forms for C_V^2 and C_T^2 in the stable outer layer.

The functional forms for C_Q^2 are the same as for C_T^2 in the surface layer and in the lower mixed layer. The location of the minimum (Fig. 2.17) would, however, fluctuate greatly depending on the relative magnitude of moisture flux from above, through entrainment, and the surface flux (Fairall, 1987).

2.9 Cospectra of turbulence

The cospectra of uw and $w\theta$ give us valuable information on the averaging times and frequency responses needed for estimating momentum flux and heat flux (the fluxes are the integrals of the cospectra from $f = 0$ to ∞ as shown in Appendix 2.1). In the surface layer we have universal curves developed from field

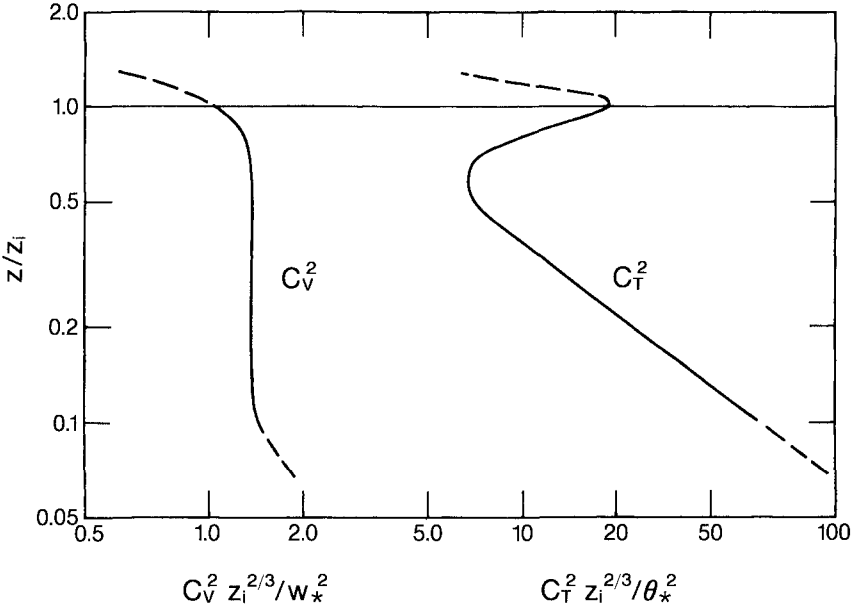$$C_V^2 \, z_i^{2/3}/w_*^2 \qquad\qquad C_T^2 \, z_i^{2/3}/\theta_*^2$$

FIG. 2.17. Vertical profiles of the normalized structure parameters in the convective boundary layer. Note that the shape of the C_T^2 profile shown follows that of γ in (2.39).

measurements (Kaimal et al., 1972) that we can use as guides for establishing the sampling and sensor response requirements for any given application.

Inertial subrange cospectral forms for uw and $w\theta$ proposed by Wyngaard and Coté (1972) show them falling off as $n^{-7/3}$ (vanishing more rapidly than the power spectra of u, w, and θ, consistent with the requirement for isotropy). In this $-7/3$ range we would expect the normalized cospectral values to be functions only of z/L and n. Their logarithmic forms, when non-dimensionalized, become

$$-\frac{fC_{uw}(f)}{u_*^2} \propto G(z/L)n^{-4/3}, \tag{2.50}$$

$$-\frac{fC_{w\theta}(f)}{u_*T_*} \propto H(z/L)n^{-4/3}, \tag{2.51}$$

where $G(z/L)$ and $H(z/L)$ are functions of z/L, determined empirically from experiments. Note that $u_*T_* = -(\overline{w'\theta'})_0$. If we hold $G(0) = H(0) = 1$, from the Kansas experiment (Kaimal et al., 1972), we have

$$-\frac{fC_{uw}(f)}{u_*^2 G(z/L)} = 0.05n^{-4.3}, \tag{2.52}$$

$$-\frac{fC_{w\theta}(f)}{u_*T_*H(z/L)} = 0.14n^{-4/3}, \tag{2.53}$$

where

$$G(z/L) = \begin{cases} 1, & -2 \leq z/L \leq 0 \\ 1 + 7.9z/L, & 0 \leq z/L \leq 2 \end{cases} \tag{2.54}$$

$$H(z/L) = \begin{cases} 1, & -2 \leq z/L \leq 0 \\ 1 + 6.4z/L, & 0 \leq z/L \leq 2. \end{cases} \tag{2.55}$$

The universal curves for the two cospectra are combined in Fig. 2.18. In stable air the cospectral curves separate systematically according to z/L as the spectra did in earlier figures, whereas the unstable cospectra crowd into a narrow band that straddles the neutral cospectrum. For convenience, we take the $z/L = 0+$ curves for uw and $w\theta$ as the cospectral forms for the unstable surface layer ($0 \leq z/L \leq -2$). These curves can be approximated by

$$-\frac{fC_{uw}(f)}{u_*^2} = \frac{12n}{(1 + 9.6n)^{7/3}}, \tag{2.56}$$

$$-\frac{fC_{w\theta}(f)}{u_*T_*} = \begin{cases} \dfrac{11n}{(1 + 13.3n)^{7/4}} & \text{for} \quad n \leq 1.0 \\ \dfrac{4n}{(1 + 3.8n)^{7/3}} & \text{for} \quad n \geq 1.0. \end{cases} \tag{2.57}$$
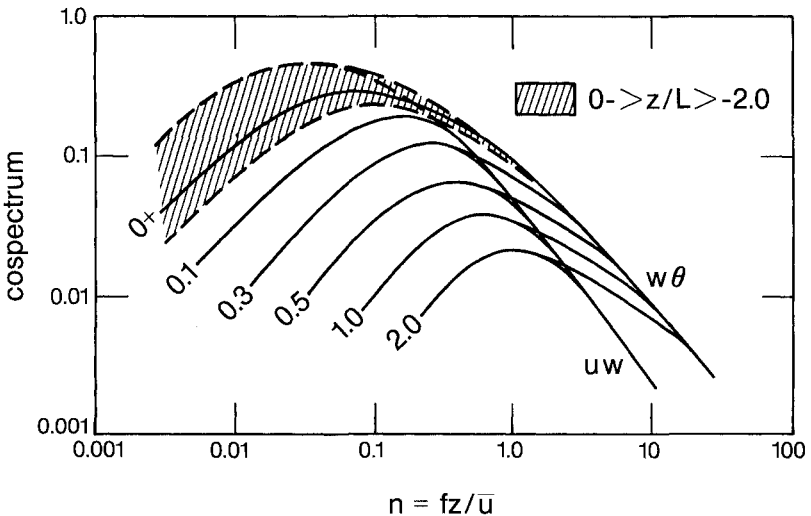

FIG. 2.18. Normalized surface layer cospectra of uw and $w\theta$, as represented in (2.52) and (2.53), shown varying with z/L. Note that the $w\theta$ cospectrum attains $-4/3$ behavior at a higher frequency than uw.

We can see from Fig. 2.18 that the two cospectra exhibit similar behavior at $n < 0.5$ (i.e., $\lambda > 2z$). They attain $-7/3$ behavior at different frequencies, however, about an octave higher in $w\theta$ than in uw. The extended range in $w\theta$ implies that the smaller eddies ($\lambda \sim z$) transport heat more effectively than momentum, pointing to the need for higher frequency response in surface layer measurements of heat flux compared to momentum flux. [On the basis of available evidence (e.g., Schmitt et al., 1979), we can assume that cospectra of w with scalars like moisture will exhibit the same shape and characteristics as the $w\theta$ cospectrum, and require sensors that are equally fast for flux measurement.]

The variation of the uw and $w\theta$ cospectral peaks with z/L is represented by a single curve in Fig. 2.19. In stable air it follows the same trend observed earlier in the velocity and temperature spectra (Fig. 2.9). In unstable air there is little, if any, variation with z/L, as one might surmise from Fig. 2.18.

As we move up into the mixed layer ($0.1z_i < z < z_i$) where the fluxes of momentum and heat are typically small and even change sign, as in the case of heat flux (Fig. 1.10), the cospectra become increasingly unpredictable. Often they show large excursions in both directions with no well-defined envelopes; the fluxes we measure are merely small differences between upward and downward transport located in different frequency bands (Kaimal et al., 1976). This is particularly true for the heat flux cospectra in which the balance shifts gradually with height until at about $0.8z_i$ the downward transport from entrainment begins to dominate. [Caughey and Kaimal (1977) found evidence of $(\lambda_m)_{w\theta}$ approaching $1.5z_i$ in the lower mixed layer.] Baroclinicity introduces similar uncertainties in stress cospectra. As a result, we have no universal forms to present for the mixed layer. Cospectral forms for the outer stable layer also tend to be unpredictable, but this
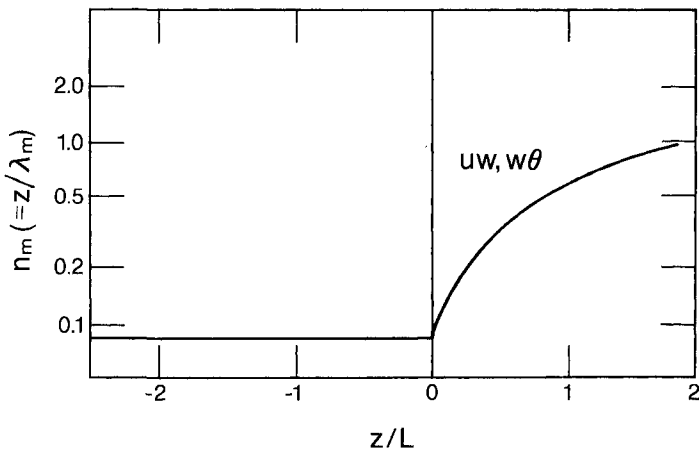

FIG. 2.19. Nondimensionalized frequency at the cospectral maxima shown as a function of z/L.

comes as no surprise given the very low levels of turbulence and the evolving nature of flow in that layer (Caughey et al., 1979).

Appendix 2.1   Fourier spectra: Essential formulas and relationships

A.2.1.1 *Fourier transform pair*

The three-dimensional energy spectrum $E_{ij}(\boldsymbol{\kappa})$ and the covariance tensor $R_{ij}(\mathbf{r})$ for homogeneous flow form a Fourier transform pair that is usually expressed as

$$E_{ij}(\boldsymbol{\kappa}) = \frac{1}{(2\pi)^3} \iiint\limits_{-\infty}^{\infty} R_{ij}(\mathbf{r}) e^{-i\boldsymbol{\kappa}\cdot\mathbf{r}} \, d\mathbf{r} \qquad (2.58a)$$

$$R_{ij}(\mathbf{r}) = \iiint\limits_{-\infty}^{\infty} E_{ij}(\boldsymbol{\kappa}) e^{i\boldsymbol{\kappa}\cdot\mathbf{r}} \, d\boldsymbol{\kappa}. \qquad (2.58b)$$

(For inhomogeneous flow, both the spectrum and the covariance tensor will be functions of the position vector $\mathbf{x}$ as well, as expressed in Section 2.1.)

A.2.1.2 *Energy spectrum*

The sum of the diagonal components of $R_{ij}(0)$ is twice the turbulent kinetic energy e:

$$R_{ii}(0) = \overline{u'^2} + \overline{v'^2} + \overline{w'^2} = 2e. \qquad (2.59)$$

From (2.58b) we have

$$R_{ii}(0) = \iiint\limits_{-\infty}^{\infty} E_{ii}(\boldsymbol{\kappa}) \, d\boldsymbol{\kappa}, \qquad (2.60)$$

which leads to the definition of spectral density as twice the contribution to turbulent kinetic energy from an element of wavenumber space $d\boldsymbol{\kappa}$.

The directional information in $E_{ii}(\boldsymbol{\kappa})$ can be removed by integrating over a spherical shell in wavenumber space of radius $\kappa = |\boldsymbol{\kappa}|$. This operation defines the energy spectrum $E(\kappa)$:

$$E(\kappa) = \frac{1}{2} \oiint E_{ii}(\boldsymbol{\kappa}) \, d\sigma, \qquad (2.61)$$

where $d\sigma$ is an element of the shell and 1/2 is included to ensure that

$$\int\limits_{0}^{\infty} E(\kappa) \, d\kappa = e.$$

A.2.1.3 *One-dimensional covariances and spectra*

The most commonly measured covariances are those with separations in the x direction (r_1) since those can be replaced with a time delay (ξ) using Taylor's frozen turbulence hypothesis

$$r_1 = \overline{u}\xi.$$

The *autocovariance* function for variable $\alpha\,(= u, v,$ or $w)$

$$R_\alpha(r_1) = \overline{\alpha'(x) \cdot \alpha'(x + r_1)} \tag{2.62a}$$

becomes

$$R_\alpha(\xi) = \overline{\alpha'(t) \cdot \alpha'(t + \xi)}. \tag{2.62b}$$

The Fourier transforms of $R_\alpha(r_1)$ and $R_\alpha(\xi)$ are the one-dimensional spectra of α' in the wavenumber and frequency domains, respectively. These are two-sided spectra we identify with a $\wedge$ to distinguish them from the one-sided power spectra we deal with in this chapter and elsewhere:

$$\hat{F}_\alpha(\kappa_1) = \frac{1}{2\pi} \int\limits_{-\infty}^{\infty} R_\alpha(r_1)e^{-i\kappa_1 r_1}\, dr_1, \tag{2.63a}$$

$$\hat{S}_\alpha(\omega) = \frac{1}{2\pi} \int\limits_{-\infty}^{\infty} R_\alpha(\xi)e^{-i\omega\xi}\, d\xi, \tag{2.63b}$$

where $\kappa_1\,(= 2\pi f\,/\overline{u})$ is the wavenumber component in the streamwise (x) direction, and $\omega\,(= 2\pi f\,)$ is the angular frequency. Their inverse transforms have the form

$$R_\alpha(r_1) = \int\limits_{-\infty}^{\infty} \hat{F}_\alpha(\kappa_1)e^{i\kappa_1 r_1}\, d\kappa_1, \tag{2.64a}$$

$$R_\alpha(\xi) = \int\limits_{-\infty}^{\infty} \hat{S}_\alpha(\omega)e^{i\omega\xi}\, d\omega. \tag{2.64b}$$

The two spectra are related through Taylor's hypothesis

$$\hat{F}_\alpha(\kappa_1) = \overline{u}\hat{S}_\alpha(\omega). \tag{2.65}$$

The type of spectrum we deal with in atmospheric work and in many engineering applications is the one-sided power spectrum $S_\alpha(f)$ such that

$$\int\limits_0^\infty S_\alpha(f)\,df = \sigma_\alpha^2 = \int\limits_{-\infty}^\infty \hat{S}_\alpha(\omega)\,d\omega.$$

Since $S_\alpha(f)$ is the positive half of an even function, we are constrained, in the interest of preserving the variance, to have

$$S_\alpha(f) = 2\hat{S}_\alpha(f) = 4\pi\hat{S}_\alpha(\omega). \tag{2.66}$$

Note that the conversion of $\hat{S}_\alpha(f)$ to $\hat{S}_\alpha(\omega)$ requires multiplication by 2π.

A.2.1.4 *Eulerian integral length and time scales*

The autocovariance functions lead us directly to definitions of the Eulerian integral length scale Λ_α and time scale T_α:

$$\Lambda_\alpha = \frac{1}{\sigma_\alpha^2}\int\limits_0^\infty R_\alpha(r_1)\,dr_1 = \int\limits_0^\infty \rho_\alpha(r_1)\,dr_1, \tag{2.67a}$$

$$T_\alpha = \frac{1}{\sigma_\alpha^2}\int\limits_0^\infty R_\alpha(\xi)\,d\xi = \int\limits_0^\infty \rho_\alpha(\xi)\,d\xi, \tag{2.67b}$$

where $\rho(r_1)$ and $\rho(\xi)$ are the familiar *autocorrelation* functions in space and time, the normalized versions of the autocovariance functions in (2.62a) and (2.62b). As in (2.65) we have, through Taylor's hypothesis,

$$\Lambda_\alpha = \overline{u}T_\alpha. \tag{2.68}$$

We define the autocorrelation only for positive r_1's and ξ's because the autocovariance is an even function, and we have

$$\int\limits_0^\infty R_\alpha(r_1)\,dr_1 = \frac{1}{2}\int\limits_{-\infty}^\infty R_\alpha(r_1)\,dr_1. \tag{2.69}$$

The integral scales are related to the one-dimensional spectra through (2.63a,b), (2.67a,b), (2.66), and (2.69):

$$\Lambda_\alpha = \frac{1}{\sigma_\alpha^2}\int\limits_0^\infty R_\alpha(r_1)\,dr_1$$

$$= \frac{\pi}{\sigma_\alpha^2} \left[\frac{1}{2\pi} \int_{-\infty}^{\infty} R_\alpha(r_1) e^{-i\kappa_1 r_1} \, dr_1 \right] \qquad \text{at } \kappa_1 = 0$$

$$= \frac{\pi}{\sigma_\alpha^2} \hat{F}_\alpha(0) \tag{2.70}$$

$$\mathcal{T}_\alpha = \frac{\pi}{\sigma_\alpha^2} [\hat{S}(f)]_{f=0}$$

$$= \frac{1}{4\sigma_\alpha^2} [S(\omega)]_{\omega=0}. \tag{2.71}$$

(In Appendix 7.2, Chapter 7, we discuss the consequences of high-pass filtering of data which essentially removes all energy at zero frequency, forcing Λ_α and $\mathcal{T}_\alpha$, as defined here, to zero.)

A.2.1.5 *Cross covariances and cross spectra*

The cross covariance between variables α and β can be expressed as

$$R_{\alpha\beta}(r_1) = \overline{\alpha'(x) \cdot \beta'(x + r_1)}. \tag{2.72}$$

This function, unlike the autocovariance function, is not an even function. We find, in general,

$$\overline{\alpha'(x) \cdot \beta'(x + r_1)} \neq \overline{\alpha'(x + r_1) \cdot \beta'(x)},$$

and its Fourier transform has both real and imaginary parts. The cross spectrum $\hat{C}r_{\alpha\beta}(\kappa_1)$ [transform of $R_{\alpha\beta}(r_1)$] separates into real and imaginary parts:

$$\hat{C}r_{\alpha\beta}(\kappa_1) = \hat{C}_{\alpha\beta}(\kappa_1) - i\hat{Q}_{\alpha\beta}(\kappa_1)$$

$$= \frac{1}{2\pi} \int_{-\infty}^{\infty} R_{\alpha\beta}(r_1) e^{-i\kappa_1 r_1} \, dr_1. \tag{2.73}$$

The real part of the cross spectrum is the cospectrum and the imaginary part the quadrature spectrum. If $R_{\alpha\beta}(r_1)$ is split into its even and odd parts, $\hat{E}_{\alpha\beta}(r_1)$ and $\hat{O}_{\alpha\beta}(r_1)$, respectively,

$$R_{\alpha\beta}(r_1) = \hat{E}_{\alpha\beta}(r_1) + \hat{O}_{\alpha\beta}(r_1), \tag{2.74}$$

it can be shown that $\hat{C}_{\alpha\beta}(\kappa_1)$ is the Fourier transform of $\hat{E}_{\alpha\beta}(r_1)$ and $\hat{Q}_{\alpha\beta}(\kappa_1)$ the transform of $\hat{O}_{\alpha\beta}(r_1)$:

$$\hat{C}_{\alpha\beta}(\kappa_1) = \frac{1}{2\pi} \int_{-\infty}^{\infty} \hat{E}_{\alpha\beta}(r_1) e^{-i\kappa_1 r_1} \, dr_1, \tag{2.75a}$$

$$\hat{Q}_{\alpha\beta}(\kappa_1) = \frac{i}{2\pi} \int_{-\infty}^{\infty} \hat{O}_{\alpha\beta}(r_1) e^{-i\kappa_1 r_1} \, dr_1. \tag{2.75b}$$

Their transforms are, respectively,

$$\hat{E}_{\alpha\beta}(r_1) = \int\limits_{-\infty}^{\infty} \hat{C}_{\alpha\beta}(\kappa_1)e^{i\kappa_1 r_1}\,d\kappa_1, \qquad (2.76a)$$

$$\hat{O}_{\alpha\beta}(r_1) = -i\int\limits_{-\infty}^{\infty} \hat{Q}_{\alpha\beta}(\kappa_1)e^{i\kappa_1 r_1}\,d\kappa_1. \qquad (2.76b)$$

$\hat{O}_{\alpha\beta}(r_1)$ makes no contribution to $R_{\alpha\beta}(0)$. Hence, from (2.76b) we have

$$\overline{\alpha'\beta'} = R_{\alpha\beta}(0) = \int\limits_{-\infty}^{\infty} \hat{C}_{\alpha\beta}(\kappa_1)\,d\kappa_1. \qquad (2.77)$$

The one-sided cospectrum $C_{\alpha\beta}(f)$ used in our discussions is defined such that

$$\int\limits_{0}^{\infty} C_{\alpha\beta}(f)\,df = \overline{\alpha'\beta'}.$$

Appendix 2.2   Taylor's hypothesis in the atmospheric boundary layer

Taylor's frozen turbulence hypothesis enables us to convert temporal measurements at a point to spatial patterns in space through the transformation $x = \overline{u}t$. Implicit is the assumption that the turbulent field is frozen in time and transported horizontally past the observer. Frequency scales become wavenumber scales $(\kappa_1 = 2\pi f/\overline{u})$, but the spectra remain unchanged in their shapes as well as their magnitudes.

We know, however, that atmospheric turbulence is neither frozen (it evolves with time) nor transported precisely at local mean wind speeds. The former fact we ignore because, typically, the eddy life times are long compared to their travel time across the sensor. The latter we usually ignore on the basis of correlation studies conducted by early investigators (Lumley and Panofsky, 1964). The high degree of consistency in the time-averaged statistics and spectra observed over the years has served to reinforce that practice.

There is, however, ample evidence of eddy convection velocities departing from $\overline{u}$, the local mean wind speed, in the CBL. Wilczak and Businger (1984), in their comprehensive study of eddy transport in the convective surface layer ($z < 150$ m) using tower measurements, tracked ramplike temperature structures (plumes and thermals) moving at speeds that varied from ramp to ramp; the larger structures, as a rule, moved faster than the smaller ones. The large thermals, along with their roots in the surface layer, are convected at mean mixed layer wind velocities (Davison, 1974), whereas the smaller (and shorter) plumes, sustained by local sources of warm air near the surface, travel at speeds smaller than $\overline{u}$ (Kaimal, 1974). Taken as a whole, the effective convection velocity, according to Wilczak and Businger (1984), is between 0.7 and 0.8 times the mixed layer mean wind. This is consistent with the findings of Kaimal et al. (1982), which showed 150-m tower $u, v,$ and w spectral peaks shifted to slightly lower (less than one octave) wavenumbers

compared to their aircraft counterparts. Whereas the aircraft and tower u spectra are virtually indistinguishable in their shapes and placement, the aircraft v and w spectra showed more rapid rolloff on the low-frequency side of their peaks compared to tower spectra.

Wind tunnel turbulence (neutral air) shows somewhat different behavior, as pointed out by Perry and Li (1990). In the near-wall region, they find small eddies traveling with the local mean wind, whereas larger "attached" eddies moved faster, causing u spectra from a flying hot-wire anemometer probe to shift slightly to lower frequencies. Within plant canopies, this behavior is exaggerated. Finnigan (1979), for example, measured the mean convection velocity of energy-containing eddies in a wheat canopy as 1.8 times the mean wind speed at canopy top. There is strong evidence of similar behavior over a wide range of natural and model plant canopies (Raupach et al., 1989). The behavior of large eddies in plant canopies is discussed in detail in Chapter 3.

Despite these findings, we continue to use $\overline{u}$ as the convection velocity in most boundary layer applications. This practice will continue as long as investigators find reasonably good agreement between atmospheric measurements made with moving and stationary probes.

Appendix 2.3   Low-frequency behavior of one-dimensional spectra

One-dimensional spectra of turbulence, available to us through measurements in the atmosphere, give misleading information on the behavior of three-dimensional turbulence at very low frequencies (Tennekes and Lumley, 1972) because modes of wavenumber κ traveling nearly normal to the κ_1 direction (the direction that defines the one-dimensional spectrum) appear as very low wavenumber contributions in $F_u(\kappa_1)$, $F_v(\kappa_1)$, and $F_w(\kappa_1)$. The phenomenon is analogous to measuring wave separation along the direction parallel to the shoreline when ocean waves are approaching the shoreline almost at right angles to it. As a result, the one-dimensional spectrum may show finite energy at $\kappa_1 = 0$ when, in fact, there is no energy at zero wavenumber.

Typically, the one-dimensional spectra of u, v, and w level off to a constant value at the low wavenumber end, as shown in Fig. 2.4. Interestingly enough, it is their intercept at $\kappa_1 = 0$ that transforms into the integral time scale $\mathcal{T}_\alpha$ (or Λ_α).

For the one-dimensional, one-sided power spectrum of α, the relationship between this apparent energy at $f = 0$ and $\mathcal{T}_\alpha$ can be derived directly from the relationship

$$\frac{S_\alpha(f)}{\sigma_\alpha^2} = 4 \int_0^\infty \rho_\alpha(\xi) \cos(2\pi f \xi)\, d\xi, \tag{2.78}$$

where σ_α^2 is the variance and $\rho_\alpha(\xi)$ the autocorrelation function of α (Fig. 2.2). At $f = 0$, we have

$$S_\alpha(0) = 4\sigma_\alpha^2 \int_0^\infty \rho_\alpha(\xi)\, d\xi = 4\sigma_\alpha^2 \mathcal{T}_\alpha, \tag{2.79}$$

which is the same as the relationship (2.71) derived from the two-sided spectrum. From (2.78) and (2.79) we can derive the asymptotic form for the low-frequency behavior of $f S_\alpha(f)/\sigma_\alpha^2$ in Fig. 2.10:

$$fS_\alpha(f)/\sigma_\alpha^2 = 4T_\alpha f. \tag{2.80}$$

Combining (2.80) and the asymptotic form for (2.22) as $f \to 0$, we get

$$4T_\alpha f = 0.164 f / f_0$$

or

$$f_0 \simeq \frac{1}{24T_\alpha}. \tag{2.81}$$

In the spectrum defined by (2.22), the peak occurs at frequency $f_m \simeq 3.8 f_0$, which leads us to the relationship

$$(f_m)_\alpha \simeq \frac{1}{6.3 T_\alpha}$$

or

$$(\lambda_m)_\alpha \simeq 6.3 \Lambda_\alpha. \tag{2.82}$$

For the hypothetical spectrum with $\rho_\alpha(\xi) = e^{-\xi/T_\alpha}$ (Lumley and Panofsky, 1964), the peak frequency is exactly $1/2\pi T_\alpha$.

Appendix 2.4 Relationship between Kolmogorov and von Karman constants

In the formulation of (2.12) we have an implicit relationship between the Kolmogorov constant α_1 and the von Karman constant k that dictates the value of one when the other is known. In neutrally stable air, where we can assume $\phi_\epsilon = 1$, (2.12) reduces to

$$
\begin{aligned}
\frac{fS_u(f)}{u_*^2} &= \frac{\alpha_1 k^{-2/3}}{(2\pi)^{2/3}} \left(\frac{fz}{\bar{u}}\right)^{-2/3} \\
&= \frac{\alpha_1 k^{-2/3}}{3.4} (n)^{-2/3}
\end{aligned}
\tag{2.83}
$$

or

$$\alpha_1 k^{-2/3} = 3.4 \left[\frac{fS_u(f)}{u_*^2}\right] n^{2/3}. \tag{2.84}$$

In the inertial subrange, at say $n = 4$, the Kansas data (Kaimal et al., 1972) yield

$$\left[\frac{fS_u(f)}{u_*^2}\right] = 0.12 \quad \text{for} \quad z/L = 0.$$

Then

$$\alpha_1 k^{-2/3} = 3.4 \times 0.12 \times (4)^{2/3} \simeq 1.0. \tag{2.85}$$

We have in (2.85) the rationale for choosing $\alpha_1 = 0.55$ to match the now accepted value of $k = 0.4$ in place of the $\alpha_1 = 0.5, k = 0.35$ combination used with the Kansas data. The formulations of the inertial subrange relationships in (2.13), (2.15), and (2.16) remain unchanged. The choice of $\alpha_1 = 0.55$ does, however, alter the coefficient for the structure function of velocity in (2.42). The new value is 2.2 instead of the generally used value of 2.0.

Frenzen (1973), who pointed out the connection between the two constants, used a different formulation. In place of u_*^2 he used the wind profile equivalent $(kz\,\partial\overline{u}/\partial z)^2$ to get $\alpha_1 k^{4/3} = 0.136$ in the logarithmic layer under neutral conditions. Frenzen's present estimate (personal communication) for $\alpha_1 k^{4/3}$, based on a reexamination of his wind profile measurements, falls between 0.16 and 0.17. A value of 0.162 is consistent with choosing $\alpha_1 = 0.55$ and $k = 0.4$.

References

Batchelor, G. K., 1960: *The Theory of Homogeneous Turbulence*. Cambridge University Press, Cambridge, 197 pp.

Caughey, S. J., and J. C. Kaimal, 1977: Vertical heat flux in the convective boundary layer. *Quart. J. Roy. Meteor. Soc., 103*, 811–815.

Caughey, S. J., and S. G. Palmer, 1979: Some aspects of turbulence structure through the depth of the convective boundary layer. *Quart. J. Roy. Meteor. Soc., 105*, 811–827.

Caughey, S. J., J. C. Wyngaard, and J. C. Kaimal, 1979: Turbulence in the evolving stable boundary layer. *J. Atmos. Sci., 36*, 1041–1052.

Corrsin, S., 1951: On the spectrum of isotropic temperature fluctuations in an isotropic turbulence. *J. Appl. Phys., 22*, 469–473.

Davison, D. S., 1974: The translation velocity of convective plumes. *Quart. J. Roy. Meteor. Soc., 100*, 572–592.

Dubovikov, M. M., and V. I. Tatarskii, 1987: Calculation of the asymptotic form of spectrum of locally isotropic turbulence in the viscous range. *Soviet Phys. J. Exp. Theor. Phys., 66* (English translation by the American Institute of Physics, 1988, 1136–1141).

Fairall, C. W., 1987: A top-down and bottom-up diffusion model for C_T^2 and C_Q^2 in the entraining convective boundary layer. *J. Atmos. Sci., 44*, 1010–1017.

Finnigan, J. J., 1979: Turbulence in waving wheat. I. Mean statistics and honami. *Bound.-Layer Meteor., 16*, 181–211.

Finnigan, J. J., F. Einaudi, and D. Fua, 1984: The interaction between an internal gravity wave and turbulence in the stably stratified nocturnal boundary layer. *J. Atmos. Sci., 41*, 2409–2436.

Frenzen, P., 1973: The observed relation between the Kolmogorov and von Kármán constants in the surface boundary layer. *Bound.-Layer Meteor., 3*, 348–358.

Hill, R. J., 1978: Models of the scalar spectrum for turbulent advection. *J. Fluid Mech., 88*, part 3, 541–562.

Højstrup, J., 1982: Velocity spectra in the unstable boundary layer. *J. Atmos. Sci., 39*, 2239–2248.

Kaimal, J. C., 1973: Turbulence spectra, length scales and structure parameters in the stable surface layer. *Bound.-Layer Meteor., 4*, 289–309.

Kaimal, J. C., 1974: Translation speed of convective plumes in the atmospheric surface layer. *Quart. J. Roy. Meteor. Soc., 100*, 46–52.

Kaimal, J. C., 1978: Horizontal velocity spectra in an unstable surface layer. *J. Atmos. Sci.,* *35,* 18–24.

Kaimal, J. C., and Y. Izumi, 1965: Vertical velocity fluctuations in a nocturnal low-level jet. *J. Appl. Meteor., 4,* 576–584.

Kaimal, J. C., R. A. Eversole, D. H. Lenschow, B. B. Stankov, P. H. Kahn, and J. A. Businger, 1982: Spectral characteristics of the convective boundary layer over uneven terrain. *J. Atmos. Sci., 39,* 1098–1114.

Kaimal, J. C., J. C. Wyngaard, Y. Izumi, and O. R. Coté, 1972: Spectral characteristics of surface layer turbulence. *Quart. J. Roy. Meteor. Soc., 98,* 563–589.

Kaimal, J. C., J. C. Wyngaard, D. A. Haugen, O. R. Coté, Y. Izumi, S. J. Caughey, and C. J. Readings, 1976: Turbulence structure in the convective boundary layer. *J. Atmos. Sci., 33,* 2152–2169.

Kolmogorov, A. N., 1941: The local structure of turbulence in incompressible viscous fluid for very large Reynolds numbers. *Doklady ANSSSR, 30,* 301–304.

Lumley, J. L., and H. A. Panofsky, 1964: *The Structure of Atmospheric Turbulence.* Wiley-Interscience, New York, 239 pp.

Moraes, O. L. L., 1988: The velocity spectra in the stable surface layer. *Bound.-Layer Meteor., 43,* 223–230.

Okamoto, M., and E. K. Webb, 1970: Temperature fluctuations in stable stratification. *Quart. J. Roy. Meteor. Soc., 96,* 591–600.

Perry, A. E., and J. D. Li, 1990: Experimental evidence for the attached-eddy hypothesis in zero pressure gradient turbulent boundary layers. *J. Fluid Mech., 218,* 405–438.

Raupach, M. R., J. J. Finnigan, and Y. Brunet, 1989: Coherent eddies in vegetation canopies. *Proc. Fourth Australian Conference on Heat and Mass Transfer,* Christchurch, New Zealand, 9–12 May 1989, 75–90.

Schmitt, K. F., C. A. Friehe, and C. H. Gibson, 1979: Structure of marine surface layer turbulence. *J. Atmos. Sci., 36,* 602–618.

Tatarski, V. I., 1961: *Wave Propagation in a Turbulent Medium* (translation from Russian by R. A. Silverman). McGraw-Hill, New York, 285 pp.

Tennekes, H., and J. L. Lumley, 1972: *A First Course in Turbulence.* MIT Press, Cambridge, 300 pp.

Van der Hoven, I., 1957: Power spectrum of horizontal wind speed in the frequency range from 0.0007 to 900 cycles per hour. *J. Meteor., 14,* 160–164.

Wilczak, J. M., and J. A. Businger, 1984: Large-scale eddies in the unstably stratified atmospheric surface layer. Part II: Turbulent-pressure fluctuations and budgets of heat flux, stress, and turbulent kinetic energy. *J. Atmos. Sci., 41,* 3551–3567.

Willis, G. E., and J. W. Deardorff, 1974: A laboratory model of the unstable planetary boundary layer. *J. Atmos. Sci., 31,* 1297–1307.

Wyngaard, J. C., and O. R. Coté, 1972: Cospectral similarity in the atmospheric surface layer. *Quart. J. Roy. Meteor. Soc., 98,* 590–603.

Wyngaard, J. C., Y. Izumi, and S. A. Collins, 1971: Behavior of the refractive-index-structure parameter near the ground. *J. Opt. Soc., 61,* 1646–1650.

Additional Reading

Panofsky, H. A., and J. A. Dutton, 1984: *Atmospheric Turbulence.* Wiley-Interscience, New York, 397 pp.